JACS
JOURNAL OF THE AMERICAN CHEMICAL SOCIETY

ARTICLE

pubs.acs.org/JACS

Evolution of the Structure and Chemical State of Pd Nanoparticles during the in Situ Catalytic Reduction of NO with H_2

Kristof Paredis,[†] Luis K. Ono,[†] Farzad Behafarid,[†] Zhongfan Zhang,[‡] Judith C. Yang,[‡,§] Anatoly I. Frenkel,[*,∥] and Beatriz Roldan Cuenya[*,†]

[†]Department of Physics, University of Central Florida, Orlando, Florida 32816, United States

[‡]Department of Mechanical Engineering and Materials Science and [§]Department of Chemical and Petroleum Engineering, University of Pittsburgh, Pittsburgh, Pennsylvania 15261, United States

[∥]Department of Physics, Yeshiva University, New York, New York 10016, United States

Supporting Information

ABSTRACT: An in-depth understanding of the fundamental structure of catalysts during operation is indispensable for tailoring future efficient and selective catalysts. We report the evolution of the structure and oxidation state of ZrO_2-supported Pd nanocatalysts (~5 nm) during the in situ reduction of NO with H_2 using X-ray absorption fine-structure spectroscopy and X-ray photoelectron spectroscopy. Prior to the onset of the reaction (≤120 °C), a NO-induced redispersion of our initial metallic Pd nanoparticles over the ZrO_2 support was observed, and $Pd^{\delta+}$ species were detected. This process parallels the high production of N_2O observed at the onset of the reaction (>120 °C), while at higher temperatures (≥150 °C) the selectivity shifts mainly toward N_2 (~80%). Concomitant with the onset of N_2 production, the Pd atoms aggregate again into large (6.5 nm) metallic Pd nanoparticles, which were found to constitute the active phase for the H_2-reduction of NO. Throughout the entire reaction cycle, the formation and stabilization of PdO_x was not detected. Our results highlight the importance of in situ reactivity studies to unravel the microscopic processes governing catalytic reactivity.

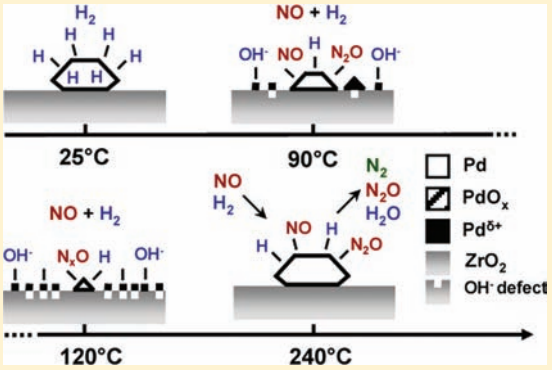

INTRODUCTION

Although in the last 2 decades significant progress has been made toward the understanding of the structure and chemical composition of supported nanoparticles (NPs) in the as-prepared state and after reaction,[1−12] much less is known about their in situ (operando) structural and chemical features and how they evolve in the course of a chemical reaction.[13−21] Reaction-induced morphological changes in NPs need to be considered, since they might lead to a decrease/increase in the relative area of the most catalytically active surface sites, as well as to changes in the chemical state of the active metal catalysts.[14−19]

The present study targets the in situ catalytic reduction of NO. This structure-sensitive reaction is of enormous industrial and environmental relevance, since NO_x emissions have significant adverse effects on the environment (acidification of rain and the generation of smog), as well as on humans (respiratory infections), and therefore, remediation through catalysis is critical.[22−28] The most common routes for the removal of NO are the selective catalytic reduction (SCR) with ammonia, CO, H_2, and hydrocarbons, as well as the direct decomposition.[4,26,29−54]

The present work focuses on the reduction of NO with H_2 (H_2-SCR).[55−57] This reaction is not as selective for N_2 as, for instance, ammonia, but it has potential technological applications due to its lower onset temperature and the fact that H_2 is readily available in exhaust streams (from the water-gas-shift reaction or from hydrocarbons).[31] Noble-metal-based catalysts are generally preferred for the H_2-SCR of NO because of their high selectivity and reduced operation temperatures.[49,58−61] Although Rh is overall catalytically better than Pd for NO-SCRs, the lower cost, higher abundance, and low-temperature activity of Pd have made it a material of choice in industrial applications.[59,62−69] A vast amount of literature is available describing the conversion and selectivity of various combinations of metal catalyst, support, and reducing agent.[4,26,29−31] However, much less attention has been paid to the optimization of the structure and oxidation state of the active catalysts, its evolution under reaction conditions, and its influence on catalytic performance.[70,71] Nevertheless, previous work has revealed the important role of the oxidation state of metal catalysts in their activity, selectivity, and stability for NO-SCRs. For example, oxidized Rh catalysts are more active for H_2-SCR than metallic Rh,[72] and NO adsorption on Cu catalysts is faster on the oxidized surface, contrary to the faster adsorption reported on the reduced surfaces of other materials such as chromia or manganese oxides.[4] Additional examples discussing the reactivity of oxidized Pd species formed under reaction conditions can be found

Received: April 22, 2011
Published: July 26, 2011

for CH_4-SCR reactions carried out in the presence of oxygen.[51,73,74] The nature of the support has also been found to influence catalytic performance either by stabilizing the NPs against coarsening, by providing additional active reaction sites, or by influencing the chemical state of the supported catalysts.[67−69,75] On acidic supports, oxidative redispersion of PdO over the support was observed, while larger PdO clusters were found on nonacidic substrates.[51,76] Dispersed Pd^{2+} cations were reported to constitute the active phase in CH_4-SCR NO reduction in the presence of O_2,[74,77,78] while NO was found to dissociate on Pd^0 sites during H_2-SCR NO reduction with O_2 in the reactant stream.[79] Furthermore, enhanced selectivities were observed when the Pd nanocatalysts were deposited on acidic zeolites or sulfated ZrO_2 supports.[80] In addition, exposure of zeolite and perovskite-supported Pd NPs to O_2 and NO was found to result in the formation of highly mobile cationic Pd species.[73,76,81−83] Finally, the size of the NPs was also shown to affect their reactivity.[84−90] For example, N_2O was not formed over small Pd NPs on SiO_2 but was present when larger clusters where used as catalysts.[89]

It is evident from the above description that a detailed knowledge of the correlation between the structure (size, shape, and dispersion on a support), chemical state of the active species, and their reactivity is indispensable for the rational design of efficient and highly selective nanocatalysts. In the present work, the H_2-SCR NO reduction over ZrO_2-supported Pd NPs has been investigated in situ via X-ray absorption fine structure (XAFS) spectroscopy and mass spectrometry, complemented with ex situ transmission electron microscopy (TEM) and X-ray photoelectron spectroscopy (XPS) measurements. XAFS allows element-specific structural and chemical analysis under operando conditions and is therefore the ideal technique to investigate the microscopic morphology of the catalysts at work and to gain insight into the structure and reaction mechanisms guiding the reduction of NO.

EXPERIMENTAL SECTION

a. Sample Preparation and Characterization. The Pd NPs were synthesized by inverse micelle encapsulation. Micellar nanocages were prepared by dissolving a nonpolar/polar diblock copolymer [polystyrene-*block*-poly(2-vinylpyridine), PS-P2VP] in toluene and subsequently loaded with a metal precursor ($C_4H_6O_4Pd$) to create encapsulated NPs. Adjusting the polymer head length (P2VP) and metal precursor−polymer head ratio (L) enables the control of the particle size. The Pd NPs in our investigation were prepared by loading PS(16000)−P2VP(3500) copolymers with a metal precursor/P2VP ratio L of 0.05. Subsequently, the NPs are impregnated on commercially available nanocrystalline (powder) ZrO_2 supports (~20 nm average grain size) by dissolving the support in the polymeric solution. The polymeric ligands are removed by annealing in an O_2 environment at 375 °C for 24 h. After this treatment, the NPs are free of carbon, as verified by XPS. The Pd loading was 1% by weight. For the TEM measurements, the Pd/ZrO_2 powders were dissolved in ethanol and subsequently drop-coated onto a carbon-coated Cu grid and dried in air.

The chemical characterization of our ZrO_2-supported Pd nanocatalysts was conducted by XPS (Al Kα, 1486.6 eV). The NPs were measured before (as-prepared) and after running the H_2-SCR NO reduction at several different temperatures for 2.5 h. At each temperature, the steady-state conversion was interrupted and the sample was transferred to the adjacent XPS ultrahigh vacuum chamber (UHV) for the measurements. The charging of the powder sample was compensated by a flood gun (4 eV) and the Zr $3d_{5/2}$ core level of ZrO_2 (182.6 eV) was used as the binding energy reference.[91] It should be noted that the Zr 3p peaks of the support overlap with the Pd 3d signals from the NPs in our samples and that all the spectra have been rescaled to yield the same Zr 3p intensity as in the bare ZrO_2 support.

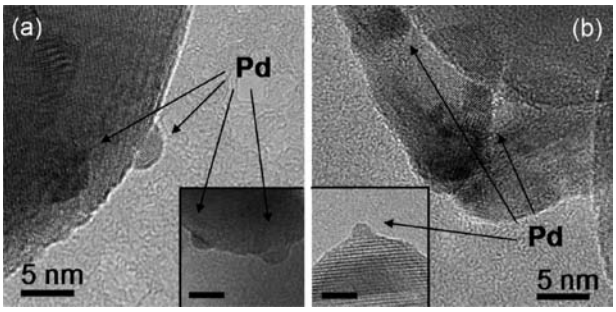

Figure 1. TEM images of micellar Pd NPs supported on ZrO_2 taken after polymer removal by an O_2-treatment before (a) and after the H_2-SCR NO reduction (b). The scale bars represent 5 nm.

b. Reactivity Data. The catalytic performance of our ZrO_2-supported Pd nanocatalysts for the reduction of NO was determined using a packed-bed mass flow reactor interfaced to a quadrupole mass spectrometer. The reactants (1% NO, 1% H_2) were introduced by employing low flow mass flow controllers and were balanced with He to provide a total flow of 25 mL/min. The catalyst bed was stepwise annealed up to 240 °C in order to determine the temperature-dependent conversion of NO and reaction selectivity via mass spectrometry. Reactivity data were acquired at each temperature under steady-state conditions. Prior to exposing the Pd NPs to the reactants, they were reduced for 1 h in a hydrogen atmosphere (40% H_2 balanced with He) at 240 °C.

c. Structural and Chemical Analysis (EXAFS, XANES). Extended X-ray absorption fine-structure (EXAFS) and near-edge structure (XANES) spectroscopy measurements were performed at the National Synchrotron Light Source (NSLS) at Brookhaven National Laboratory (beamline X18B). The experimental setup consisted of a home-built packed-bed mass flow reactor cell compatible with an in situ transmission XAFS mode and interfaced to a quadrupole mass spectrometer for the evaluation of catalytic reactivity.

At least three Pd K-edge EXAFS spectra were acquired before and after the in situ reduction of the Pd catalysts as well as at various temperatures during the H_2-SCR reaction (25−240 °C). The ATHENA software was used for averaging and aligning the spectra with the simultaneously acquired bulk Pd foil reference spectra. The smooth isolated atom background was removed using the AUTOBK algorithm.[92−94] The Fourier transformation of the (k, k^2, k^3)-weighted EXAFS data was performed via the Artemis software package, and the resulting radial distributions were fitted (first shell) with a theoretical model calculated for fcc-palladium with the FEFF6 code.[95,96] Typical k-ranges were 2.5−10 $Å^{-1}$ and r-ranges 1.5−3.0 Å. The best fit for the passive electron reduction factor of the bulk Pd reference spectrum was 0.84 and was kept constant during the analysis of all NP samples. The structural parameters extracted from the fits of the EXAFS data of our Pd/ZrO_2 catalysts under different reaction conditions are summarized in the Supporting Information (Table 1) together with fit quality factors. Examples of k- and r-space EXAFS data together with representative fits can be found in Figures 1 and 2 of the Supporting Information.

RESULTS

a. Structure, Morphological and Chemical Characterization (TEM, XPS). Representative TEM images of our ZrO_2-supported Pd NPs are shown in Figure 1 after (a) O_2 annealing at 375 °C (as-prepared) and (b) the H_2-SCR NO reduction reaction up to 240 °C. Detailed statistics of the average NP size and size distribution of this sample could not be carried out via

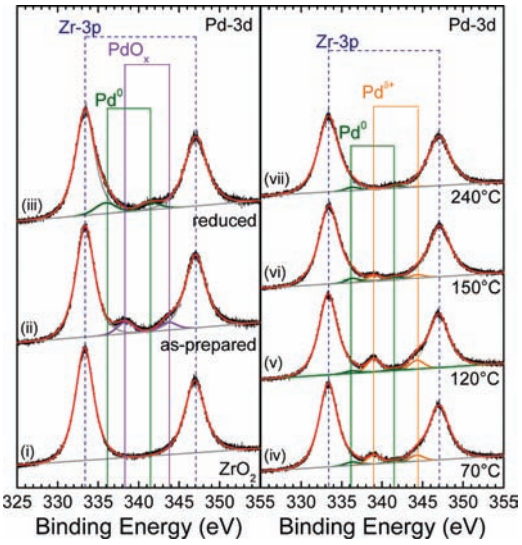

Figure 2. XPS spectra from the Pd 3d and Zr 3p core level regions taken after polymer removal by an O_2-treatment (ii), after NO reduction in H_2 (iii), and after running the H_2-SCR NO reduction at specific temperatures for approximately 2.5 h at each temperature: 70 °C (iv), 120 °C (v), 150 °C (vi), and 240 °C (vii). A reference spectrum of the Pd-free ZrO_2 support is also shown in part i. All spectra were rescaled to yield the same intensity of the Zr peaks.

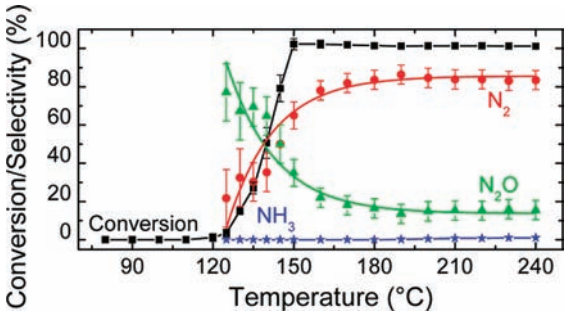

Figure 3. Conversion and selectivity data as a function of temperature for the steady state H_2-SCR NO reduction over micellar Pd NPs supported on ZrO_2.

high-angle annular dark-field scanning TEM due to the poor *Z*-contrast between the Pd NPs and the nanocrystalline ZrO_2 support. However, on the basis of the analysis of a small set of particles (∼20−30) observed in bright field images, the average size of the NPs was estimated to be 5.3 ± 1.5 nm before the reaction (as-prepared sample) and 6.5 ± 2.3 nm after the reaction. Overall, the particles were found to be rather flat, with an average width/height ratio of ∼2.2 before the reaction and ∼2.6 after the reaction, suggesting a strong NP−support interaction after our initial annealing pretreatment at 375 °C.

Figure 2 displays Pd 3d XPS data of our Pd NPs on ZrO_2 acquired before (as-prepared and reduced spectra) and after the NO reduction with H_2 at several temperatures (70, 120, 150, and 240 °C). The N 1s region is shown in Figure 3 of the Supporting Information. The sample was exposed to the reactants at each specific temperature for 2.5 h before the acquisition of the XPS spectra. Figure 2 displays two sets of core-level XPS peaks (spin−orbit doublets) corresponding to the Zr 3p and Pd 3d orbitals. The data of the Pd-free ZrO_2 support are shown in Figure 2i for reference. Two clear shoulders appear in the XPS spectrum of the as-prepared Pd sample, partially overlapping with the more prominent ZrO_2 features (Figure 2ii). On the basis of the large binding energies of these peaks (338.3 and 343.8 eV) and the fact that the sample was annealed in O_2 before these measurements, these contributions are identified as PdO_x species, reflecting the initial oxidation of our as-prepared NPs.[97] The presence of PdO_x is confirmed by XANES and EXAFS (see below). A binding energy of 336.7 eV (Pd $3d_{5/2}$) was obtained for Pd^{2+} in bulk PdO and 336.8 eV in $Pd(OH)_2$ (not shown, and ref 98), while bulk Pd metal is generally reported at 335.2 eV.[99] Binding energies in the range of 336.2−337.2 eV (Pd $3d_{5/2}$) were reported in the literature for PdO in NPs depending of the NP preparation method, NP size, and nature of the support.[100−102] More unstable oxide species such as PdO_2 have also been suggested to form on Pd NPs, with BEs ranging from 337.2 to 338.2 eV.[100−102] On the basis of our XPS data we cannot conclude whether we have PdO or PdO_2 species on our samples due to the convolution of size, support, and oxidation state effects leading to NP charging and positive BE shifts.

After the reduction in H_2 (Figure 2iii), the binding energy of the Pd $3d_{5/2}$ and $3d_{3/2}$ features decreased to 336.1 and 341.4 eV, which is attributed to the presence metallic Pd species. The higher BE of the latter species in our NPs as compared to bulk Pd (335.2 eV[99]) is attributed to size and/or charge transfer effects. With the introduction of the reactants, the Pd^0 contribution significantly decreases while a new feature appears at 339.0 eV for Pd $3d_{5/2}$ (Figure 2iv). The latter value is +0.7 larger than that observed for the initial oxidized Pd NPs (as-prepared). Interestingly, the content of the cationic Pd component was found to increase with increasing reaction temperature up to 120 °C. Under our reaction conditions, such a component might be attributed to the formation of Pd hydroxides. For example, BEs of 337.9−338.5 eV were reported for Pd^{4+} species formed under water-rich environments.[103,104]

Above 120 °C, the content of the cationic Pd feature ($Pd^{\delta+}$) was found to decrease and at 240 °C it had completely vanished, and only a small Pd^0 fraction remained visible. Interestingly, the intensity of the Pd^0 peaks was significantly lower as compared to that in the spectrum of the H_2-reduced NPs (Figure 2iii).[97] The reduction of the overall Pd signal at 240 °C can be related to several effects: (i) the loss of Pd under the influence of the reactants, (ii) the encapsulation of the Pd NPs by the ZrO_2 support or migration of Pd atoms/clusters into the ZrO_2 matrix during the reaction, and (iii) the complete reduction of the Pd NPs above 150 °C and their subsequent coarsening. The latter effects can result in the apparent disappearance or strong suppression of the Pd signal because of the stronger overlap of Pd 3d and Zr 3p features of ZrO_2 and Pd metal as compared to $Pd^{\delta+}$ and the longer mean free escape path of the photoelectrons in the coarsened NPs. On the basis of the results of the in situ XAFS measurements reported below, the only plausible possibility is (iii).

b. Catalytic Reactivity. Figure 3 summarizes the temperature dependence of the conversion of NO over the ZrO_2-supported Pd NPs under steady-state reaction conditions. The onset temperature (defined as the 50% conversion temperature, T_{50}) was found to be 140 °C, and a 100% conversion was reached at 150 °C. The reaction products observed for the H_2-SCR of NO are nitrous oxide (N_2O), nitrogen (N_2), ammonia (NH_3), and water. These products are obtained through the following

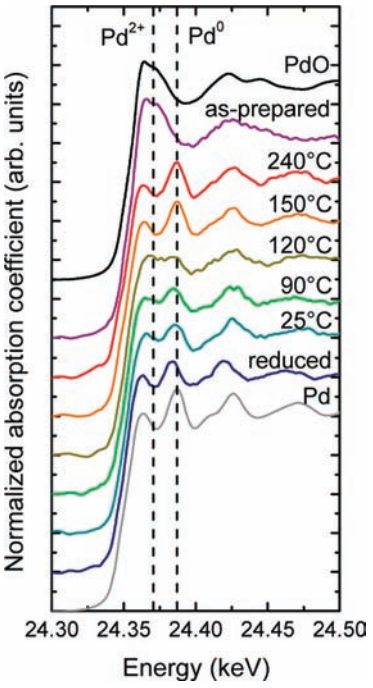

Figure 4. Pd K-edge XANES spectra recorded after polymer removal (in O_2 at 375 °C, as-prepared), after reduction (in H_2 at 240 °C), and a different temperatures during the in situ H_2-SCR NO reduction. Reference spectra for PdO and bulk Pd are shown as well.

reaction pathways:

$$NO + H_2 \rightarrow 1/2N_2 + H_2O \quad (1)$$

$$NO + 1/2H_2 \rightarrow 1/2N_2O + 1/2H_2O \quad (2)$$

$$NO + 5/2H_2 \rightarrow NH_3 + H_2O \quad (3)$$

No traces of nitrogen dioxide (NO_2) were detected in the course of the reaction. The product selectivity is also presented in Figure 3. At the onset of the NO conversion, a high selectivity (>70%) toward N_2O is observed, but it rapidly decreases with increasing temperature to a saturation level of about 15%. Simultaneously, the selectivity toward N_2 shows the opposite trend: a strong increase from less than 30% at the onset temperature for NO conversion to a maximum saturation level of ~85% at 150 °C. Above 180 °C, the third reaction pathway sets in, and a small fraction of NH_3 (<2%) is observed.

c. In Situ Evolution of the Structure and Chemical Composition of Pd NP Catalysts (XANES, EXAFS). Figure 4 displays Pd K-edge XANES spectra of ZrO_2-supported Pd NPs acquired in situ under different reaction conditions together with reference spectra for bulk metallic Pd and PdO. The K-edge XANES probes the electronic transition from the 1s to 5p orbitals and is sensitive to the chemical state of the Pd atoms. After the removal of the encapsulating polymeric ligands in oxygen at high temperature, the XANES spectrum of the NPs (labeled as-prepared) shows a strong resemblance with the reference spectrum for bulk PdO, indicating the oxidation of the NPs, which is in agreement with the XPS results in Figure 2ii showing the presence of oxidic Pd species. After the subsequent reduction treatment in H_2 at 240 °C, the complete decomposition of the Pd oxides and the

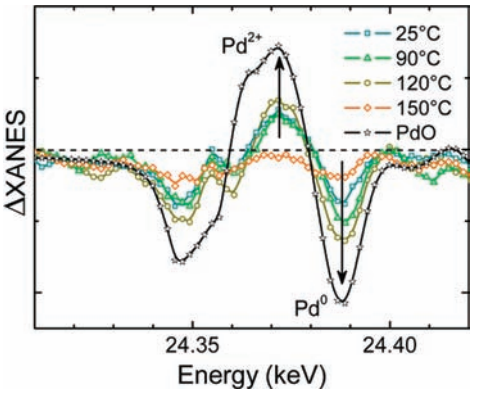

Figure 5. ΔXANES spectra obtained during various stages of the H_2-SCR NO reduction. The data correspond to XANES spectra acquired at different temperatures from which the spectrum of the bulk-like Pd foil measured at room temperature has been subtracted.

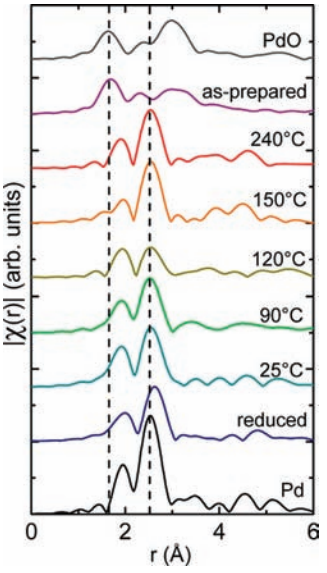

Figure 6. k^2-Weighted Fourier transform Pd K-edge EXAFS spectra (r-space) taken after reduction and during various stages of the in situ H_2-SCR NO reduction. Bulk Pd and PdO spectra are shown as reference. The k-range for the Fourier transform was $2.5 < k < 10$ Å^{-1}.

appearance of metallic Pd features are observed in the XANES spectrum measured at room temperature. The characteristic near-edge peaks, however, show a distinct shift to lower energy. Upon initial sample exposure to the reactants (NO and H_2) at room temperature, the metallic features remain but shift slightly back to higher energies. Additionally, the latter spectrum also exhibits a small feature at ~24.37 keV, indicating the presence of cationic Pd species ($Pd^{\delta+}$). The latter contribution becomes more pronounced as the temperature is further increased to 90 and 120 °C. Simultaneously, the intensity of the metallic peak at ~24.39 keV decreases significantly. These effects are more clearly visualized in Figure 5, where the ΔXANES spectra of our NPs measured at different temperatures under NO + H_2 flow are shown. The ΔXANES values displayed in Figure 5 correspond to the difference between the Pd K-edge XANES spectrum of our NPs measured at the temperatures indicated and that of bulk metallic Pd measured at room temperature. Our data

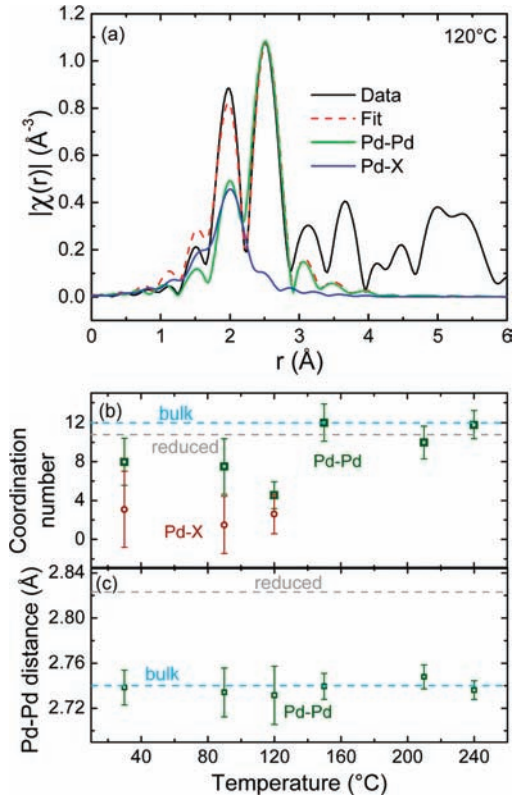

Figure 7. (a) Fourier transform Pd K-edge EXAFS spectrum (*r*-space) recorded at 120 °C, along with the total fit and the Pd−Pd and Pd−X contribution. (b) Dependence of the first nearest neighbor coordination number on the reaction temperature during the H_2-SCR NO reduction over Pd NPs supported on ZrO_2: the Pd−Pd and the Pd−X contribution obtained from the fitting of in situ EXAFS spectra are shown. The dashed gray line indicates the Pd−Pd coordination number after NP reduction in H_2 and before reactant exposure. (c) Pd−Pd bond distance as a function of temperature. The dashed gray line indicates the Pd−Pd distance after NP reduction in H_2, while the dashed blue line corresponds to the bulk value.

reveal that a $Pd^{\delta+}$ state, similar to the Pd^{2+} state in bulk PdO, appears upon introducing the reactant mixture at 25 °C, showing its maximum contribution at 120 °C. This change correlates with the gradual decrease of the metallic state with increasing temperature up to 120 °C. However, the metallic features remain present even at 120 °C, as can be seen in Figure 4 and in the EXAFS spectra shown in Figure 6.

At 150 °C, the XANES spectrum in Figure 4 changes drastically, becoming nearly identical to that of pure metallic Pd. However, no shift of the metallic Pd^0 feature to lower energy is observed with respect to the bulk Pd spectrum. The return to the metallic state is also evidenced by the nearly featureless ΔXANES spectrum observed in Figure 5 at 150 °C. As the reaction temperature is further increased up to 240 °C, no additional changes are observed, and the XANES spectra of the NPs remain very similar to those of bulk metallic Pd.

The Fourier transformed k^2-weighted Pd K-edge EXAFS data of the Pd NPs acquired in situ under different reaction conditions are displayed in Figure 6 along with reference data for bulk metallic Pd and bulk PdO. Comparing the as-prepared spectrum with the PdO reference reveals that the Pd NPs are almost completely oxidized after the polymer removal treatment, in good agreement with our XANES and XPS results. Upon reduction in H_2, the radial distribution exhibits a large resemblance with the metallic Pd state, but with a clear shift of the main features to higher distances. Upon the introduction of the reactants (NO + H_2) and the subsequent increase in temperature, the EXAFS spectra continue to exhibit characteristic metallic features, although the expansion of the Pd−Pd lattice has disappeared. Furthermore, the intensity of the main metallic Pd peak in the radial distribution at 2.5 Å (phase uncorrected) is considerably reduced at 120 °C, while the characteristic metallic Pd feature at 2 Å (phase uncorrected) did not decrease, hinting at the presence of an overlapping additional scatter pair at a shorter distance than the Pd−Pd. Further, after the initial reduction pretreatment in H_2, none of the characteristic features of Pd oxide at 1.6, 2.7, and 3.1 Å (phase uncorrected) are observed throughout the entire reaction cycle.[73] Guided by the analysis of the XANES (and also XPS) data, we attribute the second component to a Pd−X signal, where X stands for a low *Z* scatterer, i.e., N or O.

The EXAFS data were fitted with two theoretical contributions: one originating from Pd in a metallic environment (Pd−Pd) and a second component corresponding to cationic Pd atoms (Pd−X) with a large starting value of the Pd−X distance of 2.5 Å, which was subsequently varied in the fit. A representative fit is shown in Figure 7a for EXAFS data acquired at 120 °C under reaction conditions. The fits yield information on the first nearest neighbor (1st NN) coordination numbers (N_{Pd-Pd}, N_{Pd-X}, Figure 7b) and the corresponding distances (d_{Pd-Pd}, d_{Pd-X}, Figure 7c) for each spectrum. The details on the fit results and related fit quality parameters are presented in Table 1 of the Supporting Information. The respective values for the H_2-reduced NPs (i.e., the starting configuration) and a bulk Pd reference are shown by the dashed lines. After NP reduction in H_2, a Pd−Pd coordination of 10.8 ± 0.9 and a distance of 2.82 ± 0.01 Å were obtained. When the reactants are first injected into the gaseous stream, the Pd−Pd 1st NN coordination slightly decreases, while the average Pd−Pd distance returns to its bulk-like value of 2.74 Å. With increasing reaction temperature, the coordination number further decreases to 5.6 ± 2.0 at 120 °C. Despite the presence of a reducing reaction environment, a small cationic Pd−X contribution appears after the introduction of the reactants at room temperature (2.55 ± 0.08 Å), concomitant with the decrease of the initial H_2 flow from 50% H_2 in He to 1% H_2 + 1% NO in He. According to the changes observed in the EXAFS spectra, the relative content of the latter component was found to increase with increasing temperature up to 120 °C. We will elaborate on the origin of this component in the Discussion below. At 150 °C, the Pd−X contribution disappears and the Pd−Pd coordination number shows a sudden increase to 12.0 ± 1.9, consistent with the return to the pure metallic state, as indicated by XANES. Above 150 °C, the coordination number remains constant within the uncertainty. After the introduction of the reactants, the average Pd−Pd distance was found to be rather stable throughout the entire reaction cycle, as shown in Figure 7c.

■ DISCUSSION

The onset temperature T_{50} for the reduction of NO with H_2 over micellar Pd NPs supported on ZrO_2 was found to be 140 °C. Once the conversion reaches 100%, the activity remains stable with increasing temperature up to 240 °C. At the onset of the reaction, the catalyst shows low selectivity toward N_2, with N_2O being the main reaction product. The N_2 selectivity was found to increase with increasing reaction temperature, reaching ~80% at

150 °C when 100% NO conversion is achieved. No changes were observed in the selectivity of our catalysts above 150 °C. Our Pd NPs have a considerably lower onset reaction temperature as compared to Pd(111), where NO conversion was only observed above 200 °C.[105] Interestingly, Pd/Al_2O_3 catalysts from Yang et al. showed already 100% NO conversion (with pure H_2) at 70 °C, but the N_2 selectivity remained below 50%.[65] Barrera et al. reported onset temperatures of 80−175 °C for $Pd/Al_2O_3-La_2O_3$ catalysts, although their N_2 selectivity did not exceed 60%.[106] Granger et al.[49] described onset reaction temperatures of ∼100 °C for Pd/Al_2O_3 catalysts, with 50% N_2 selectivity only above 300 °C, with the parallel production of NH_3 resulting in a decrease in activity.[49] Similar Pd catalysts supported on $LaCoO_3$ exhibited a higher onset temperature (160 °C) but showed a stable activity at high temperature, with a N_2 selectivity above 50% at 200 °C.[67] Overall, our catalysts show a stable selectivity and activity pattern. Interestingly, a relatively low amount of NH_3 is produced throughout our entire reaction cycle (<2%), even at high temperatures. Significant NH_3 formation is often associated with H_2-rich reaction conditions, and as such, our low NH_3 production might be at least partially due to our relatively low H_2 concentration (i.e., NO:H_2 of 1:1). However, even in experiments with stoichiometric concentrations, considerable NH_3 formation is reported in the literature for similar catalysts,[49,67] indicating that the specific nature of our micelle-based catalysts (size, shape, substrate dispersion, and support) also plays a major role in the observed selectivity.[67] According to previous studies, the conversion and selectivity of H_2-SCR catalysts might be further improved by fine-tuning the inlet concentrations. For instance, reaction conditions involving excess H_2 are known to result in an increase of the NO conversion, but they also facilitate the production of undesired NH_3.[105] In order to suppress the formation of ammonia, additional oxygen is often fed to the reactant stream or a second metal is added to the catalyst formulation. However, such modifications might also heavily compromise the overall activity, selectivity, and temperature window of operation.[49,65,66,68,69] The optimization of the inlet reactant concentrations and catalyst composition will be the subject of future research for our micelle-based materials.

Contrary to the majority of the previous works, where the structural and chemical composition of the catalysts was only available in the as-prepared and reacted states, our in situ XAFS investigation allows one to follow its evolution in the course of the NO reduction. This enables one to establish structure, chemical state, and reactivity correlations. Prior to the reactant exposure, our Pd NPs were reduced in H_2 (240 °C), which leads to a clear lattice expansion due to the formation of Pd hydride species.[107] The observed expansion in the Pd−Pd distances of ∼3.1% is in agreement with previous studies.[108−110] The large (∼11) 1st NN coordination number obtained by EXAFS for the reduced NPs evidence the presence of large metallic Pd NPs, in agreement with our TEM data (∼5.3 nm average NP size).[107,111] Upon the introduction of the reactants (NO + H_2) at room temperature, the average Pd−Pd distance was found to decrease significantly, returning to the bulk Pd value and suggesting the complete decomposition of the hydride. Furthermore, our XANES data clearly reveal the appearance of a large fraction of a $Pd^{\delta+}$ component (Figure 5 and Pd−X component in Figure 7), along with a concomitant strong suppression of the Pd^0 contribution. With increasing temperature, the relative content of the $Pd^{\delta+}$ component increases significantly at the expense of the Pd^0 contribution, as can be deduced from the ΔXANES spectra in Figure 5. The $Pd^{\delta+}$ or Pd−X contribution observed cannot be simply attributed to the formation of Pd−O bonds in a palladium oxide phase. In fact, the EXAFS spectra measured at the corresponding temperatures do not exhibit the features characteristic of PdO (i.e., the peaks at 1.65, 2.70, and 3.15 Å in the phase-shift uncorrected radial distribution of Figure 6).[76,83,112] Furthermore, our surface-sensitive XPS data revealed a +0.7 eV increase in the BE of the cationic Pd species detected in our sample under reaction conditions (e.g., after reaction at 120 °C) as compared to the as-prepared oxidized sample (Figure 2). This result indicates a different chemical environment for the $Pd^{\delta+}$ species as compared to the initial PdO_x. As shown in Figure 3 of the Supporting Information, small N signals were detected via XPS as well, indicating that N-species might play a role in the formation of cationic Pd species. However, we cannot conclude from the present data if such species would also be stable on the sample during the reaction above room temperature, since the XPS data were acquired ex-situ after cooling down the sample to room temperature.

The fits of our EXAFS data acquired below 150 °C reveal the existence of a Pd−X component with an average bond length of ∼2.55 ± 0.08 Å. On the basis of available literature, this bond can be assigned to a long Pd−O bond, for example, due to the adsorption of H_2O. In fact, distances between 2.37 and 2.59 Å have been reported for $Pd(OH)_2$.[113,114] A related possibility for a long Pd−O bond was proposed by Koningsberger and Gates,[12] who reported large metal−O distances (2.5−2.7 Å) for atoms within NPs in contact with O from the underlying oxide support when the samples were treated in H_2 below 350 °C or when the supports were hydroxylated. Hydrogen is suggested to reduce the charge on the metal, which leads to a longer metal−support O distance. Our experimental findings can be explained following the former idea, since our samples were measured at low temperature (<240 °C) in a reactant stream containing H_2 and under water-rich experimental conditions, which are expected to lead to the hydroxylation of the oxide support. Following Koningsberger and Gates,[12] we tentatively identify the location of hydrogen atoms at the NP/support interface, likely in the form of OH^- species. Such a model explains the observation of cationic Pd in the XANES and XPS data and the long Pd−X pair in EXAFS.

Our XAFS data reveal that a large fraction of the Pd atoms in our NPs reside in a nonmetallic environment ($Pd^{\delta+}$) under reactant exposure in the temperature range from 25 to 120 °C. This is evidenced by the increase in the intensity of the XANES absorption peak ($Pd^{\delta+}$) and the decrease in the metallic Pd−Pd scattering, which is accompanied by an increase of the additional Pd−X component (Figure 7b). The presence of a large fraction of $Pd^{\delta+}$ is also confirmed by our XPS measurements up to 150 °C. In addition, a strong decrease in the Pd−Pd coordination number is observed in parallel with the appearance of the Pd−X bonding. These effects suggest that our NPs undergo significant chemical and morphological changes at these temperatures. It should also be considered that due to the initial large size of our Pd NPs (∼5 nm according to TEM), the volume-averaged EXAFS technique is not very sensitive to changes in the NP surface, and therefore, the strong modifications in the EXAFS spectra reported here must reflect drastic changes in the morphology and/or chemical composition of the NPs affecting a large number of atoms. The reactant-mediated structural changes extracted from the analysis of our EXAFS spectra might be attributed to the encapsulation of the Pd NPs by the ZrO_2 support. However, this effect is not consistent with our data; i.e., there is no concomitant deactivation, and Pd−Zr bonds are not observed. Furthermore, ZrO_2 decomposition has only been reported above 500 °C.[115,116] A second

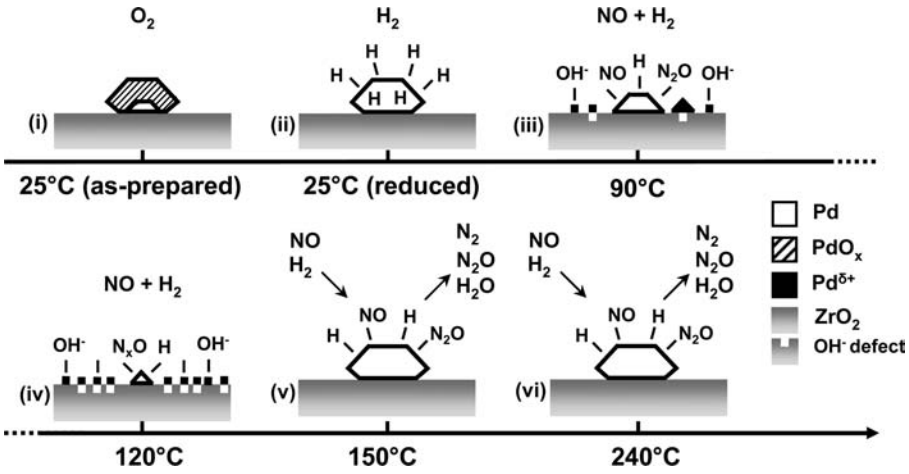

Figure 8. Schematic representation of the structure and chemical state of our Pd nanocatalysts at various stages of the H_2-SCR NO reduction.

possibility is the NO-induced disruption and redispersion of the Pd particles over the support, leading to individual ions or small clusters on the ZrO_2 surface. The low Pd−Pd CN obtained at 120 °C and the detection of an additional interface/surface component [Pd−X] can be easily explained if Pd redispersion is considered. The appearance of cationic Pd species in the XPS spectra and the significant increase in their BE (+0.7 eV) with respect to the PdO_x species available in the oxidized as-prepared samples also suggest that smaller cationic Pd clusters are present on our samples upon reactant exposure. The phenomenon of NP redispersion on oxide supports has been previously reported by a number of groups, including NO-induced redispersion of Pd NPs.[73,74,76,81−83,117,118] For example, Okumura et al.[73,76] demonstrated that the oxidation of Pd NPs at high temperature leads to NP disintegration and the formation of dispersed PdO. The acidic nature of the support, giving rise to a strong interaction with the more basic PdO, was found to underlie this effect. The oxidative redispersion of Pd NPs by NO adsorption at room temperature on Pd^0 was proven by Che et al.[78] and Aylor et al.[82,118] They showed the decomposition of NO upon adsorption on the Pd crystallites and their subsequent oxidation:

$$2NO_{(ads)} \rightarrow N_2O + O \quad (4)$$

$$Pd^0 + O \rightarrow Pd^{2+}O^{2-} \quad (5)$$

The resulting Pd ions are known to be highly mobile due to the strong interaction with the acidic support, which facilitates their redispersion over the support surface as single ions or small clusters[82,83,118] The O^{2-} ions produced in process 5 might not remain bonded to the Pd^{2+} cations, but they may react with H_2, leading to Pd−OH complexes (e.g., Pd−OH_2, with a Pd−O distance in agreement with our EXAFS observation)[82,118] In fact, it was shown that protons are required to stabilize the Pd^{2+} ions on zeolite surfaces.[77,119] These can be provided by an acidic support or by H_2, in the form of OH groups.[119] The ZrO_2 used in the present study is only weakly acidic, and therefore, the H_2 available within the reactant stream or that initially absorbed on/in the Pd NPs (spilling over to the support) might play an important role in the stabilization of the Pd^{2+} ions.[120,121] We note that the time scale (48 h) for the complete dispersion of 2 nm Pd crystallites under NO exposure reported by Che et al. is consistent with the progressive redispersion observed for our NPs with increasing annealing temperature (room temperature to 120 °C).[118]

As the NO conversion reaches 100% at 150 °C, both XANES and EXAFS data show a pure metallic Pd spectrum. Consequently, the Pd−X contribution has completely vanished at this temperature (see Figure 6). Moreover, the Pd−Pd coordination number of ∼12 ± 2 at 150 °C demonstrates the formation of large Pd^0 clusters. The reduction and aggregation of the Pd^{2+} ions into stable metallic particles during NO conversion are likely to be a consequence of the desorption of the oxidative species (N_2O and H_2O) and was previously shown to occur in a H_2 atmosphere during the NO reduction with CH_4 above 330 °C.[74,83] Furthermore, if our $Pd^{\delta+}$ species were stabilized at OH defects on the ZrO_2 surface, their stability will depend on the relative coverage of such species on the ZrO_2 surface under the different reaction conditions, which is expected to decrease with increasing annealing temperature.[122] The favorable role of OH species on the stabilization of small physical vapor deposited metal NPs supported on oxides against coarsening has been previously reported.[75,123,124]

The reduction and agglomeration of the Pd NPs in the present study above 120 °C correlate with the shift of the reaction selectivity from N_2O toward N_2. This is in accordance with previous results indicating that the formation of N_2 is mainly governed by metallic Pd sites.[49,74,79,106,125,126] Accordingly, our in situ XAFS data indicate that the active catalyst for the selective reduction of NO using H_2 are large (∼5 nm) metallic NPs. However, it should be noted that, in the XPS spectrum of Figure 2vi, a small $Pd^{\delta+}$ contribution is still visible at 150 °C, which suggests that not all Pd atoms in our sample are metallic at that point. Nevertheless, only metallic Pd species were found to be present in our sample by XPS above 150 °C. Since EXAFS is a volume-averaging technique, it is not as sensitive as XPS to small changes in the chemical state of atoms at the surface of NPs, which explains the lack of clear Pd−X contribution at 150 °C.

Further increasing the reaction temperature up to 240 °C has no significant impact on the reactivity and selectivity of our Pd NPs, aside from the minor additional generation of NH_3. Above 150 °C, the XANES and EXAFS spectra remain nearly identical, indicating the lack of significant structural changes in our samples at these temperatures (see Figure 6). This is reflected in the Pd−Pd coordination numbers and the Pd−Pd distances, which are constant within the uncertainty. At this point, XPS shows that the Pd species

are completely reduced. Furthermore, on the basis of a comparison of the initial (after reduction in H_2 but before the reaction) and final (after the reaction, i.e., after the NP disruption and subsequent reagglomeration) Pd−Pd 1st NN CN numbers, the average particle size was found to remain nearly constant, although a slight increase might have occurred. Nevertheless, the increase in the CNs observed after the reaction is within the error bars. The analysis of the TEM images in Figure 1 also revealed similar NP size distributions before and after the reaction, with a possible increase in the NP diameter after the reaction, which is also within the error margin of the corresponding NP size distribution.

After exposing our Pd NPs to the reactants for an extended period of time (18 h) at 240 °C, no decrease in catalytic activity was observed. This is evidence that our catalysts did not suffer from poisoning by oxides or N-containing intermediates.

The in situ structural and chemical information obtained for our Pd/ZrO_2 system via XAFS also allows us to gain insight into the origin of the disappearance of the Pd 3d signal from our XPS data at 240 °C (Figure 2). The loss of Pd is disregarded due to the lack of changes in the overall XAFS signal (e.g., absorption edge jump). The hypothesis of encapsulation of Pd by ZrO_2 and subsequent Zr−Pd alloy formation is also disregarded, since no Pd−Zr bonds were observed via EXAFS and ZrO_2 is known to decompose only above 500 °C, which is significantly higher than our maximum reaction temperature.[115,116] Therefore, the disappearance of the Pd features from the XPS spectrum in Figure 2vii is assigned to the reduction of the cationic Pd species to metallic Pd. The fact that a lower Pd signal (no clear signal) is detected at the end of the reaction via XPS as compared to that measured before the reaction but after H_2 reduction is assigned to the decrease in the BE of the metallic Pd species present in this sample, which leads to an even stronger overlap between ZrO_2 and Pd photoelectron peaks. Such decrease in the BE suggests the presence of larger NPs after the redispersion and reagglomeration, which is in agreement with the TEM data and the slightly higher Pd−Pd CN obtained at 240 °C.

The evolution of the structure, morphology, and chemical state of our Pd nanocatalysts at different stages of the H_2-SCR NO reduction is summarized in Figure 8: (i) the initial oxidized state; (ii) the reduced particles with absorbed H; (iii) the exposure to the reactants at 90 °C with the subsequent redispersion and stabilization of cationic Pd species, which are likely to be formed upon interaction of Pd with OH^- groups on the ZrO_2 support; (iv) the maximum redispersion at 120 °C; (v) the change in the chemical state of the NPs back to metallic coinciding with their agglomeration and the conversion of NO to N_2O and N_2 at 150 °C and (vi) at 240 °C.

CONCLUSIONS

The evolution of the structure and oxidation state of ZrO_2-supported Pd nanocatalysts during the in situ reduction of NO with H_2 has been monitored using X-ray absorption spectroscopy and photoelectron spectroscopy. Our results show that our catalysts undergo significant structural and chemical changes. In particular, cationic Pd species are detected upon the introduction of the reactants. Furthermore, the redispersion of the Pd nanoparticles on the ZrO_2 surface and the formation of small Pd clusters or ions was observed upon the introduction of the reactants (NO + H_2) at room temperature until the onset temperature for NO reduction was reached (120 °C). This phenomenon is the result of the interaction of NO with surface atoms in the initially metallic Pd clusters supported on ZrO_2. Both EXAFS and XPS data indicate the formation of $Pd^{\delta+}$ species at the expense of Pd^0 from room temperature to 120 °C. Nevertheless, our EXAFS data indicate that PdO_x species are not formed but that the cationic Pd species are likely stabilized at OH defects on the ZrO_2 surface. Possibly due to the redispersion phenomenon, a high selectivity for N_2O was detected at the onset of the NO reduction reaction (≥120 °C). As the reaction temperature increases (>150 °C), the selectivity shifts mainly toward N_2 (∼80%). Concomitant with the onset of the NO reduction reaction, the disappearance of the $Pd^{\delta+}$ species and formation of larger metallic Pd aggregates are observed, evidencing that metallic Pd constitutes the active phase for the H_2-reduction of NO over Pd NPs on ZrO_2.

In conclusion, our results emphasize the importance of in situ structural and chemical information under operation conditions for the understanding of the mechanisms governing catalytic reactivity. The significant morphological changes observed in the current study can be exploited to tailor the next generation of selective catalysts.

ASSOCIATED CONTENT

Supporting Information. (i) EXAFS fit parameters, (ii) representative EXAFS spectra (*k*- and *r*-space) with the corresponding fits in *r*-space, and (iii) XPS spectra of the N 1s core-level region. This material is available free of charge via the Internet at http://pubs.acs.org/.

AUTHOR INFORMATION

Corresponding Authors
roldan@ucf.edu; anatoly.frenkel@yu.edu

ACKNOWLEDGMENT

The authors are grateful to Dr. Jason R. Croy (UCF) for assistance in sample preparation, YoungWoo Joh (UCF) for preliminary reactivity tests, and beamline support by Dr. Nebojsa Marinkovic (BNL). Reactivity and in situ XAFS studies were supported by the National Science Foundation (NSF-DMR-1006232). Partial travel support was provided by DOE's Synchrotron Catalysis Consortium (DE-FG02-05ER15688). Electron microscopy studies were funded by DOE BES (DE-FG02-03ER15476). NFCF at the University of Pittsburgh is acknowledged for the use of JEM 2100F. Use of NSLS was supported by DOE (DE-AC02-98CH10866). A.I.F. would like to thank Prof. A. Datye for bringing ref 12 to his attention. B.R.C. would like to thank Prof. H.-J. Freund for kindly hosting her sabbatical research stay at the Fritz-Haber-Institute (Berlin, Germany), where part of the manuscript was written.

REFERENCES

(1) Henry, C. R. *Prog. Surf. Sci.* **2005**, *80*, 92–116.
(2) Roldan Cuenya, B. *Thin Solid Films* **2010**, *518*, 3127–3150.
(3) Freund, H.-J. *Angew. Chem., Int. Ed.* **1997**, *36*, 452–475.
(4) Parvulescu, V. I.; Grange, P.; Delmon, B. *Catal. Today* **1998**, *46*, 233–316.
(5) Somorjai, G. A.; Park, J. Y. *Angew. Chem., Int. Ed.* **2008**, *47*, 9212–9228.
(6) Zaera, F. *J. Phys. Chem. Lett.* **2010**, *1*, 621–627.
(7) Santra, A. K.; Goodman, D. W. *J. Phys.: Condens. Matter* **2003**, *15*, R31–R62.

(8) Freund, H.-J. *Surf. Sci.* **2007**, *601*, 1438–1442.
(9) Bell, A. T. *Science* **2003**, *14*, 1688–1691.
(10) Norskov, J. K.; Bligaard, T.; Rossmeisl, J.; Christensen, C. H. *Nat. Chem.* **2009**, *1*, 37–46.
(11) Mostafa, S.; Behafarid, F.; Croy, J. R.; Ono, L. K.; Li, L.; Yang, J. C.; Frenkel, A. I.; Roldan Cuenya, B. *J. Am. Chem. Soc.* **2010**, *132*, 15714–15719.
(12) Koningsberger, D. C.; Gates, B. C. *Catal. Lett.* **1992**, *14*, 271–277.
(13) McKenna, K. P.; Shluger, A. L. *J. Phys. Chem. C* **2007**, *111*, 18848–18852.
(14) Newton, M. A.; Belver-Coldeira, C.; Martinez-Arias, A.; Fernandez-Garcia, M. *Nat. Mater.* **2007**, *6*, 528–532.
(15) Newton, M. A.; Michiel, M. D.; Kubacka, A.; Fernandez-Garcia, M. *J. Am. Chem. Soc.* **2010**, *132*, 4540–4541.
(16) Nolte, P.; Stierle, A.; Jin-Phillip, N. Y.; Kasper, N.; Schulli, T. U.; Dosch, H. *Science* **2008**, *321*, 1654–1658.
(17) Mittendorfer, F.; Seriani, N.; Dubay, O.; Kresse, G. *Phys. Rev. B* **2007**, *76*, 233413.
(18) Giorgio, S.; Cabie, M.; Henry, C. R. *Gold Bull.* **2008**, *41*, 167–173.
(19) Giorgio, S.; Sao Joao, S.; Nitsche, S.; Chaudenson, D.; Sitja, G.; Henry, C. R. *Ultramicroscopy* **2006**, *106*, 503–507.
(20) Paredis, K.; Ono, L. K.; Mostafa, S.; Li, L.; Zhang, Z.; Yang, J.; Barrio, L.; Frenkel, A. I.; Roldan Cuenya, B. *J. Am. Chem. Soc.* **2011**, *133*, 6728–6735.
(21) Hansen, P. L.; Wagner, J. B.; Helveg, S.; Rostrup-Nielsen, J. R.; Clausen, B. S.; Topsoe, H. *Science* **2002**, *295*, 2053–2055.
(22) Crutzen, P. J.; Brohl, C. *J. Phys. Chem. A* **2000**, *105*, 1579–1582.
(23) Ravishankara, A. R. *Chem. Rev.* **2003**, *103*, 4505–4508.
(24) Chiron, M.; Crucq, A.; Frennet, A. In *Studies in Surface Science and Catalysis*; Elsevier: New York, 1987; Vol. 30, pp 1−10.
(25) Mauzerall, D. L.; Sultan, B.; Kim, N.; Bradford, D. F. *Atmos. Environ.* **2005**, *39*, 2851–2866.
(26) Fritz, A.; Pitchon, V. *Appl. Catal., B* **1997**, *13*, 1–25.
(27) Fenger, J. *Atmos. Environ.* **2009**, *43*, 13–22.
(28) Geddes, J. A.; Murphy, J. G.; Wang, D. K. *Atmos. Environ.* **2009**, *43*, 3407.
(29) Hu, Y.; Griffiths, K.; Norton, P. R. *Surf. Sci.* **2009**, *603*, 1740–1750.
(30) Roy, S.; Hegde, M. S.; Madras, G. *Appl. Energy* **2009**, *86*, 2283–2297.
(31) Shelef, M. *Catal. Rev. Sci. Eng.* **1975**, *11*, 1–40.
(32) Amiridis, M. D.; Zhang, T. J.; Farrauto, R. J. *Appl. Catal., B* **1996**, *10*, 203–227.
(33) Busca, G.; Lietti, L.; Ramis, G.; Berti, F. *Appl. Catal., B* **1998**, *18*, 1–36.
(34) Armor, J. N. *Catal. Today* **1995**, *26*, 147–158.
(35) Burch, R.; Breen, J. P.; Meunier, F. C. *Appl. Catal., B* **2002**, *39*, 283–303.
(36) Burch, R. *Catal. Rev. Sci. Eng.* **2004**, *46*, 271–333.
(37) Breen, J. P.; Burch, R. *Top. Catal.* **2006**, *39*, 53–58.
(38) Centi, G.; Perathoner, S. *Catal. Today* **2009**, *148*, 191–205.
(39) Gandhi, H. S.; Graham, G. W.; McCabe, R. W. *J. Catal.* **2003**, *216*, 433–442.
(40) Garin, F. *Catal. Today* **2004**, *89*, 255–268.
(41) Garin, F. *Appl. Catal., A* **2001**, *222*, 183–219.
(42) Heck, R. M. *Catal. Today* **1999**, *53*, 519–523.
(43) Traa, Y.; Burger, B.; Weitkamp, J. *Microporous Mesoporous Mater.* **1999**, *30*, 3–41.
(44) McCabe, R. W.; Kisenyi, J. M. *Chem. Ind.-London* **1995**, 605–608.
(45) Liu, Z.-P.; Jenkins, S. J.; King, D. A. *J. Am. Chem. Soc.* **2004**, *126*, 7336–7340.
(46) Sengupta, D.; Adams, J. B.; Schneider, W. F.; Hass, K. C. *Catal. Lett.* **2001**, *74*, 193–199.
(47) Bosch, H.; Janssen, F. *Catal. Today* **1988**, *2*, 369–379.
(48) Janssen, F.; Meijer, R. *Catal. Today* **1993**, *16*, 157–185.
(49) Granger, P.; Dhainaut, F.; Pietrzik, S.; Malfoy, P.; Mamede, A.; Leclercq, L.; Leclercq, G. *Top. Catal.* **2006**, *39*, 65–76.
(50) Cho, B. K. *J. Catal.* **1994**, *148*, 697–708.
(51) Ali, A.; Alvarez, W.; Loughran, C. J.; Resasco, D. E. *Appl. Catal., B* **1997**, *14*, 13–22.
(52) Lombardo, E. A.; Sill, G. A.; d'Itri, J. L.; Hall, W. K. *J. Catal.* **1998**, *173*, 440–449.
(53) Miyadera, T. *Appl. Catal., B* **1993**, *2*, 199–205.
(54) Klingstedt, F.; Eränen, K.; Lindfors, L. E.; Andersson, S.; Cider, L.; Landberg, C.; Jobson, E.; Eriksson, L.; Ilkenhans, T.; Webster, D. *Top. Catal.* **2004**, *30−31*, 27–30.
(55) Hecker, W. C.; Bell, A. T. *J. Catal.* **1985**, *92*, 247–259.
(56) de Wolf, C. A.; Nieuwenhuys, B. E. *Catal. Today* **2001**, *70*, 287–300.
(57) Frank, B.; Emig, G.; Renken, A. *Appl. Catal., B* **1998**, *19*, 45–57.
(58) Getman, R. B.; Schneider, W. F. *J. Phys. Chem. C* **2006**, *111*, 389–397.
(59) Shelef, M.; Gandhi, H. S. *Ind. Eng. Chem. Prod. Res. Dev.* **1972**, *11*, 393–396.
(60) Taylor, K. C.; Klimisch, R. L. *J. Catal.* **1973**, *30*, 478–484.
(61) Pirug, G.; Bonzel, H. P. *J. Catal.* **1977**, *50*, 64–76.
(62) Rempel, J.; Greeley, J.; Hansen, L. B.; Nielsen, O. H.; Norskov, J. K.; Mavrikakis, M. *J. Phys. Chem. C* **2009**, *113*, 20623–20631.
(63) Kobylinski, T. P.; Taylor, B. W. *J. Catal.* **1974**, *33*, 376–384.
(64) Roy, S.; Hegde, M. S.; Sharma, S.; Lalla, N. P.; Marimuthu, A.; Madras, G. *Appl. Catal., B* **2008**, *84*, 341–350.
(65) Yang, J.-B.; Fu, O.-Z.; Wu, D.-Y.; Wang, S.-D. *Appl. Catal., B* **2004**, *49*, 61–65.
(66) Miller, D. D.; Chuang, S. S. C. *J. Phys. Chem. C* **2009**, *113*, 14963–14971.
(67) Dhainaut, F.; Pietrzyk, S.; Granger, P. *Appl. Catal., B* **2007**, *70*, 100–110.
(68) Ueda, A.; Nakao, T.; Azuma, M.; Kobayashi, T. *Catal. Today* **1998**, *45*, 135–138.
(69) Macleod, N.; Cropley, R.; Keel, J. M.; Lambert, R. M. *J. Catal.* **2004**, *221*, 20–31.
(70) Meng, M.; Lin, P.; Fu, Y. *Catal. Lett.* **1997**, *48*, 213–222.
(71) Okumura, K.; Yoshimoto, R.; Suzuki, K.; Niwa, M. *Bull. Chem. Soc. Jpn.* **2005**, *78*, 361–366.
(72) Savatsky, B. J.; Bell, A. T. *ACS Symp. Ser.* **1982**, *178*, 105–141.
(73) Okumura, K.; Niwa, M. *J. Phys. Chem. B* **2000**, *104*, 9670–9675.
(74) Lobree, L. J.; Aylor, A. W.; Reimer, J. A.; Bell, A. T. *J. Catal.* **1999**, *181*, 189–204.
(75) Brown, M. A.; Carrasco, E.; Sterrer, M.; Freund, H.-J. *J. Am. Chem. Soc.* **2010**, *132*, 4064–4065.
(76) Okumura, K.; Amano, J.; Yasunobu, N.; Niwa, M. *J. Phys. Chem. B* **2000**, *104*, 1050–1057.
(77) Adelman, B. J.; Sachtler, W. M. H. *Appl. Catal., B* **1997**, *14*, 1–11.
(78) Ogura, M.; Hayashi, M.; Kikuchi, E. *Catal. Today* **1998**, *45*, 139–145.
(79) Macleod, N.; Cropley, R.; Lambert, R. M. *Catal. Lett.* **2003**, *86*, 69–75.
(80) Chin, Y. H.; Pisanu, A.; Serventi, L.; Alvarez, W. E.; Resasco, D. E. *Catal. Today* **1999**, *54*, 419–429.
(81) Nishihata, Y.; Mizuki, J.; Akao, T.; Tanaka, H.; Uenishi, M.; Kimura, M.; Okamoto, T.; Hamada, N. *Nature* **2002**, *418*, 164–167.
(82) Aylor, A. W.; Lobree, L. J.; Reimer, J. A.; Bell, A. T. *J. Catal.* **1997**, *172*, 453–462.
(83) Okumura, K.; Yoshimoto, R.; Uruga, T.; Tanida, H.; Kato, K.; Yokota, S.; Niwa, M. *J. Phys. Chem. B* **2004**, *108*, 6250–6255.
(84) Boccuzzi, F.; Guglielminotti, E.; Martra, G.; Cerrato, G. *J. Catal.* **1994**, *146*, 449–459.
(85) Hierl, R.; Urbach, H. P.; Knozinger, H. *J. Chem. Soc. Faraday Trans.* **1992**, *88*, 355–360.
(86) Fornasiero, P.; Dimonte, R.; Rao, G. R.; Kaspar, J.; Meriani, S.; Trovarelli, A.; Graziani, M. *J. Catal.* **1995**, *151*, 168–177.
(87) Murota, T.; Hasegawa, T.; Aozasa, S.; Matsui, H.; Motoyama, M. *J. Alloys Compd.* **1993**, *193*, 298–299.
(88) Oh, S. H.; Eickel, C. C. *J. Catal.* **1991**, *128*, 526–536.
(89) Xu, X. P.; Goodman, D. W. *Catal. Lett.* **1994**, *24*, 31–35.

(90) Chien, S.-H.; Kuo, M.-C.; Lu, C.-H.; Lu, K.-N. *Catal. Today* **2004**, *97*, 121–127.
(91) Crist, B. V. In *Handbook of Monochromatic XPS Spectra—Commercially Pure Binary Oxides*; XPS International, Inc.: 2005; Vol. 2, p 828.
(92) Ravel, B.; Newville, M. *J. Synchrotron Radiat.* **2005**, *12*, 537–541.
(93) Newville, M.; Livins, P.; Yacoby, Y.; Rehr, J. J.; Stern, E. A. *Phys. Rev. B* **1993**, *47*, 14126–14131.
(94) Newville, M. *J. Synchrotron Radiat.* **2001**, *8*, 322–324.
(95) Zabinsky, S. I.; Rehr, J. J.; Ankudinov, A.; Albers, R. C.; Eller, M. J. *Phys. Rev. B* **1995**, *52*, 2995–3009.
(96) Setthapun, W.; Williams, W. D.; Kim, S. M.; Feng, H.; Elam, J. W.; Rabuffetti, F. A.; Poeppelmeier, K. R.; Stair, P. C.; Stach, E. A.; Ribeiro, F. H.; Miller, J. T.; Marshall, C. L. *J. Phys. Chem. C* **2010**, *114*, 9758–9771.
(97) Croy, J. R.; Mostafa, S.; Hickman, L.; Heinrich, H.; Roldan Cuenya, B. *Appl. Catal., A* **2008**, *350*, 207–216.
(98) Pillo, T.; Zimmermann, S.; Steiner, P.; Hufner, S. *J. Phys.: Condens. Matter* **1997**, *9*, 3987–3999.
(99) Moulder, J. F.; Stickle, W. F.; Sobol, P. E.; Bomben, K. D. Perkin-Elmer Corp.: Eden Prairie, MN, 1992; Vol. 3.
(100) Nolte, P.; Stierle, A.; Balmes, O.; Srot, V.; van Aken, P. A.; Jeurgens, L. P. H.; Dosch, H. *Catal. Today* **2009**, *145*, 243–250.
(101) Semagina, N.; Renken, A.; Laub, D.; Kiwi-Minsker, L. *J. Catal.* **2007**, *246*, 308–314.
(102) Kibis, L. S.; Titkov, A. I.; Stadnichenko, A. I.; Koscheev, S. V.; Boronin, A. I. *Appl. Surf. Sci.* **2009**, *255*, 9248–9254.
(103) Moroseac, M.; Skála, T.; Veltruská, K.; Matolín, V.; Matolínová, I. *Surf. Sci.* **2004**, *566−568*, 1118–1123.
(104) Kim, K. S.; Gossmann, A. F.; Winograd, N. *Anal. Chem.* **1974**, *46*, 197–200.
(105) de Wolf, C. A.; Nieuwenhuys, B. E. *Surf. Sci.* **2000**, *469*, 196–203.
(106) Barrera, A.; Viniegra, M.; Bosch, P.; Lara, V. H.; Fuentes, S. *Appl. Catal., B* **2001**, *34*, 97–111.
(107) Tew, M. W.; Miller, J. T.; van Bokhoven, J. A. *J. Phys. Chem. C* **2009**, *113*, 15140–15147.
(108) Rose, A.; Maniguet, S.; Mathew, R. J.; Slater, C.; Yao, J.; Russell, A. E. *Phys. Chem. Chem. Phys.* **2003**, *5*, 3220–3225.
(109) Davis, R. J.; Landry, S. M.; Horsley, J. A.; Boudart, M. *Phys. Rev. B* **1989**, *39*, 10580–10583.
(110) Wicke, E.; Brodowsky, H.; Zuchner, H. *Hydrogen in Metals II, Vol 29 of Topics in Applied Physics*; Springer: Berlin, 1978.
(111) Frenkel, A. I.; Hills, C. W.; Nuzzo, R. G. *J. Phys. Chem. B* **2001**, *105*, 12689–12703.
(112) Grunwaldt, J.-D.; Maciejewski, M.; Baiker, A. *Phys. Chem. Chem. Phys.* **2003**, *5*, 1481–1488.
(113) Cao, Y.; Chen, Z.-X. *Surf. Sci.* **2006**, *600*, 4572–4583.
(114) Kua, J.; Goddard, W. A. *J. Am. Chem. Soc.* **1999**, *121*, 10928–10941.
(115) Asakura, K.; Iwasawa, Y.; Purnell, S. K.; Watson, B. A.; Barteau, M. A.; Gates, B. C. *Catal. Lett.* **1992**, *15*, 317–327.
(116) Ono, L. K.; Yuan, B.; Heinrich, H.; Roldan Cuenya, B. *J. Phys. Chem. C* **2010**, *114*, 22119–22133.
(117) Homeyer, S. T.; Sachtler, W. M. H. *J. Catal.* **1989**, *117*, 91–101.
(118) Che, M.; Dutel, J. F.; Gallezot, P.; Primet, M. *J. Phys. Chem.* **1976**, *80*, 2371–2381.
(119) Rice, M. J.; Chakraborty, A. K.; Bell, A. T. *J. Catal.* **2000**, *194*, 278–285.
(120) Xiao, L.; Schneider, W. F. *Chem. Phys. Lett.* **2010**, *484*, 231–236.
(121) Ivanov, A.; Kustov, L. *Russ. Chem. Bull.* **1998**, *47*, 1061–1066.
(122) Carrasco, E.; Brown, M. A.; Sterrer, M.; Freund, H.-J.; Kwapien, K.; Sierka, M.; Sauer, J. *J. Phys. Chem. C* **2010**, *114*, 18207–18214.
(123) Jensen, M. C. R.; Venkataramani, K.; Helveg, S.; Clausen, B. S.; Reichling, M.; Besenbacher, F.; Lauritsen, J. V. *J. Phys. Chem. C* **2008**, *112*, 16953–16960.
(124) Heemeier, M.; Stempel, S.; Shaikhutdinov, S. K.; Libuda, J.; Bäumer, M.; Oldman, R. J.; Jackson, S. D.; Freund, H. J. *Surf. Sci.* **2003**, *523*, 103–110.
(125) Niemantsverdriet, J. W. *Spectroscopy in Catalysis*: VCH Verlagsgesellschaft mbH: Weinheim, Germany, 1993.
(126) Dujardin, C.; Mamede, A. S.; Payen, E.; Sombret, B.; Huvenne, J. P.; Granger, P. *Top. Catal.* **2004**, *30−31*, 347–352.